

Preconditioned Adjoint Data Assimilation for Two-dimensional Decaying Isotropic Turbulence

Hongyi Ke, Zejian You, and Qi Wang*

Department of Aerospace Engineering,

San Diego State University, San Diego, CA 92182, USA

(Dated: February 17, 2026)

Abstract

Adjoint-based data assimilation for turbulent Navier–Stokes flows is fundamentally limited by the behavior of the adjoint dynamics: in backward time, adjoint fields exhibit exponential growth and become increasingly dominated by small-scale structures, severely degrading reconstruction of the initial condition from sparse measurements. We demonstrate that the relative weighting of spectral components in the adjoint formulation can be systematically controlled by redefining the inner product under which the adjoint operator is defined. The inverse problem is formulated as a constrained minimization in which a cost functional measures the mismatch between model predictions and observations, and the adjoint equations provide the gradient with respect to the initial velocity field. Redefining the forward–adjoint duality through a Fourier-space weighting kernel preconditions the optimization and is mathematically equivalent to changing the representation of the control variable or, alternatively, introducing a smoothing operation on the governing dynamics. Specific kernel choices correspond to fractional integration or diffusion operators applied to the initial condition. Among these, exponential kernels provide effective regularization by suppressing high-wavenumber contributions while preserving large-scale coherence, leading to improved reconstruction across scales. A statistical analysis of an ensemble of adjoint fields from different turbulent realizations reveals scale-dependent backward growth rates, explaining the instability of the standard formulation and clarifying the mechanism by which the proposed preconditioning attenuates incoherent small-scale amplification.

I. INTRODUCTION

Reconstructing turbulent flows from sparse and noisy observations is a central and intrinsically challenging inverse problem in fluid dynamics [1–6], with applications in atmosphere–ocean prediction [7, 8], closed-loop flow control [9, 10], and experimental flow measurements such as particle image velocimetry (PIV) [11–13]. The difficulty arises from the high dimensionality of the flow state, the nonlinear and chaotic dynamics governed by the Navier–Stokes equations, and the limited and indirect nature of practical measurements. These features render brute-force optimization or sampling approaches computationally intractable. Ad-

* qwang4@sdsu.edu

joint methods have therefore become the standard tool for PDE-constrained data assimilation, as they enable efficient evaluation of gradients of the cost functional with respect to high-dimensional control variables at a computational cost comparable to that of a forward simulation [14–16]. Beyond gradient evaluation, adjoint-based sensitivity analysis continues to play an important role in data-driven flow reconstruction and in providing physical insight into flow receptivity and observability [17–19]. Several fundamental questions remain unresolved, including the appropriate choice of inner product for defining adjoint duality for different flow setups [18, 20, 21], the integration of physical constraints with data-driven information, and the regularization of adjoint sensitivities in turbulent regimes [22]. Addressing these issues is essential before adjoint-based methods can be robustly deployed in practical high-Reynolds-number applications.

In the classical 4D-Var setting, the simulation tries to minimize the mismatch between the predicted measurements and the true observations. The gradient of the mismatch with respect to the initial condition (or other control variables) is obtained by solving the adjoint of the forward dynamics [11, 23, 24], at a cost on the same order as a forward simulation and essentially independent of the state dimension [14–16]. For large-scale simulations, accurate gradient computation requires an adjoint consistent with the numerical discretization, including boundary conditions and mesh metrics, which has been derived and validated for many data-assimilation applications [19, 25]. Practical implementations rely on checkpointing and incremental/outer-loop strategies to manage storage burden [16, 26]. The appeal of adjoint-based assimilation is primarily its scalability: the work per gradient does not scale with the number of control variables, enabling PDE-constrained optimization in very large systems—provided the backward integration remains numerically stable, and the computed sensitivities remain physically meaningful. Besides evaluating the gradient, the sensitivity field calculated from adjoint Green’s functions and its ensemble average can be utilized to detect dangerous events with uncertainty quantification [17, 24, 27, 28], or optimize sensor placements [29].

When applied to turbulence, gradient-based approaches built upon the governing equations encounter fundamental difficulties. Turbulent flows are intrinsically multiscale and chaotic: nonlinear energy transfer populates a broad range of wavenumbers, and nearby initial conditions diverge exponentially in time. The adjoint system inherits this sensitivity but evolves backward in time; consequently, perturbations aligned with the leading Lyapunov

directions amplify exponentially and progressively concentrate at small scales [5, 30]. Direct examinations of adjoint dynamics in wall-bounded and isotropic turbulence show rapid amplification of adjoint energy and steep spectral tilting toward high wavenumbers, yielding ill-conditioned gradients over long assimilation windows [22, 31]. This behavior is consistent with the Lyapunov spectrum of turbulent flows and explains why naive extensions of 4D-Var to long windows can diverge even when the forward solution is well resolved [32]. In practice, the resulting gradients overfit incoherent small-scale content, bias reconstructions, and mask the recovery of large-scale structures; moreover, fundamental observability limits, e.g., from wall-based measurements, underline the difficulty of inferring full-field turbulence from limited data [19, 33]. Together, these findings motivate scale-aware formulations that temper adjoint growth while preserving the physically relevant components of the sensitivity.

A variety of remedies have been proposed to temper adjoint growth while retaining reconstruction fidelity. Classical approaches impose *a priori* smoothness or scale penalties on the control, e.g., Tikhonov/Sobolev regularization [34, 35], and apply spectral filtering to suppress high-wavenumber noise; these stabilize the optimization but may attenuate physically meaningful small scales or introduce bias. A related line of research has recognized that regularization can be achieved not only by augmenting the cost functional, but also by modifying the inner products (or “brackets”) used in the derivation of adjoint-based algorithms. In particular, Scott Collis *et al.* [20] pointed out that altering certain brackets appearing in the adjoint formulation may introduce a regularizing effect, leading to smoother and more numerically tractable gradients. Similar ideas were discussed in Heinkenschloss and Vicente [36] and later Protas *et al.* [21]. Bayesian and ensemble-based schemes (e.g., hybrid/EnVar or Kriging-enhanced formulations) incorporate prior uncertainty and reduce sensitivity to local gradient pathologies at increased computational cost [26, 37, 38]. It is also possible to change the solution space to effectively constrain the search within meaningful function space, constructed either by known prior distributions or through data-based methods, such as an auto-encoder [39–41]. Related stabilization ideas include synchronization/nudging and observability-aware formulations that respect fundamental limits of what can be inferred from restricted measurements [19, 42]. The open challenge is to design scale-aware procedures that simultaneously improve adjoint stability, maintain physical fidelity across wavenumbers, and remain computationally tractable for high-Reynolds-number flows.

Recent advances in scientific machine learning provide alternative strategies for such

inverse problems in fluid mechanics. Physics-informed neural networks (PINNs) [43, 44] incorporate governing equations as soft constraints in neural-network training and have been applied to data assimilation and flow reconstruction without explicitly forming adjoint equations. Similarly, operator-learning frameworks such as DeepONet [45] and Fourier neural operators [46] aim to approximate solution operators directly from data, enabling rapid inference once trained. More recently, diffusion and score-based generative models [47–49] have been adapted to physics-constrained inverse problems, where stochastic sampling in a learned latent space implicitly imposes a data-driven prior on the reconstructed fields. While these approaches have demonstrated promising reconstruction capabilities, they typically rely on learned representations whose spectral properties and stability characteristics are not explicitly linked to the dynamical structure of the Navier-Stokes equations. In particular, they do not directly address the backward Lyapunov growth [19, 31, 50, 51] that underlies adjoint instability in turbulent flows, but rather mitigate ill-posedness through data-driven priors or stochastic regularization. Moreover, large-scale turbulent regimes remain challenging due to training cost, generalization limits, and the difficulty of embedding discretization-consistent numerical operators within deep architectures.

These developments highlight an emerging theme: successful reconstruction in turbulence requires both physical principles and an informed treatment of how information is distributed across scales in the flow field. Building on these insights, the present work formulates the inner-product modification explicitly in Fourier space through a scale-dependent kernel, and interprets it as a linear transformation of the control variable that reweights its components in wavenumber space during optimization. Conceptually, the kernel acts as a tunable spectral filter that balances sensitivity across wavenumbers, mitigating the small-scale amplification that plagues backward integration while preserving energetically and dynamically relevant motions. From an optimization perspective, this scale-dependent reweighting is equivalent to a spectral preconditioning of the adjoint system with respect to the initial condition. Building on a discrete adjoint Navier-Stokes solver, we derive the preconditioned adjoint equations, establish the relation between adjoint variables defined under different inner products, and formulate the optimization in terms of the transformed control variable to improve the conditioning of the data assimilation problem. We further provide a statistical analysis of the adjoint sensitivity to reveal the scale-dependent growth behavior, which clarifies the mechanism of the precondition kernel and indicates pathways

for future extensions to more complex turbulent flows. We demonstrate this method on two-dimensional decaying isotropic turbulence, where standard, regularized, and preconditioned formulations are compared across different kernel choices.

The remainder of the paper is organized as follows. Section II A derives the adjoint equations within the data-assimilation framework. Section II B introduces generalized inner products and establishes the corresponding transformation between adjoint variables. In §II C, we show that this modification is equivalent to a change of control variable or, alternatively, to introducing a precursor smoothing operation, thereby formulating the preconditioned data-assimilation framework. Section III A verifies the equivalence between altering the representation of the initial condition and redefining the inner product. Sections III C and III D investigate spectral preconditioning based on algebraic and exponential kernels, respectively, and compare their performance with the standard adjoint formulation. Section IV provides a statistical analysis of adjoint sensitivity for pointwise measurements, elucidating the scale-dependent growth mechanisms underlying the proposed stabilization. Concluding remarks and future directions are given in §V.

II. MATHEMATICAL FORMULATION

We first introduce the standard adjoint equations derived from the optimization using the forward two-dimensional Navier-Stokes equations as constraints, then derive the dependence of the adjoint gradient on the definition of the inner product, which is equivalent to preconditioning in the optimization procedure.

A. Adjoint-based Data Assimilation

Suppose the velocity field $\mathbf{u}(\mathbf{x}, t)$ is a realization of decaying two-dimensional homogeneous isotropic turbulence, satisfying the two-dimensional incompressible Navier-Stokes equations in non-dimensional form,

$$\begin{aligned} \frac{\partial \mathbf{u}}{\partial t} + (\mathbf{u} \cdot \nabla) \mathbf{u} &= -\nabla p + \nu \nabla^2 \mathbf{u}, \\ \nabla \cdot \mathbf{u} &= 0, \quad \mathbf{u}|_{t=0} = \mathbf{u}_0. \end{aligned} \tag{1}$$

Here, $\nu = \frac{1}{Re} = \frac{\nu^*}{U^* L^*}$ denotes the non-dimensional kinematic viscosity. The superscript $*$ denotes dimensional quantities, where U^* , L^* , and ν^* are the dimensional characteristic velocity, length, and kinematic viscosity of the flow, respectively. The non-dimensional pressure is denoted as p . The initial condition $\mathbf{u}(t = 0) = \mathbf{u}_0$ is the goal of the data assimilation.

Suppose the measurement kernel is denoted as \mathcal{M} , the measurements can be obtained by applying the measurement kernel on the reference evolution of velocity, namely $\mathbf{m} = \mathcal{M}(\mathbf{u}_r)$, with \mathbf{u}_r being the reference field solved with the true initial condition $\mathbf{u}_{0,r}$. We construct the cost function as the norm of the mismatch between the modeled observation $\mathcal{M}(\mathbf{u})$ and the true measurement \mathbf{m} ,

$$\mathcal{J} = \frac{1}{2} \|\mathcal{M}(\mathbf{u}) - \mathbf{m}\|^2. \quad (2)$$

In some circumstances, we would like to utilize an augmented cost function by a Sobolev-type regularization on the initial condition to penalize high-wavenumber content and improve the conditioning of the inverse problem,, namely

$$\mathcal{J} = \frac{1}{2} \|\mathcal{M}(\mathbf{u}) - \mathbf{m}\|^2 + \frac{\lambda}{2} \int_{\Omega} |\nabla \mathbf{u}_0|^2 d\Omega, \quad (3)$$

with λ being a small positive parameter for the regularization. Either way, the goal is to minimize the loss function \mathcal{J} with the equations 1 as constraints.

We construct the Lagrangian using the Lagrange multiplier \mathbf{u}^\dagger and p^\dagger , which are also the adjoint velocity and pressure,

$$\mathcal{L} = \mathcal{J} - \int_0^T \left[\frac{\partial \mathbf{u}}{\partial t} + (\mathbf{u} \cdot \nabla) \mathbf{u} + \nabla p - \nu \nabla^2 \mathbf{u}, \mathbf{u}^\dagger \right] dt - \int_0^T [\nabla \cdot \mathbf{u}, p^\dagger] dt. \quad (4)$$

Here the square brackets $[\cdot, \cdot]$ denote a spatial inner product defined as

$$[\mathbf{a}, \mathbf{b}] = \int_{\Omega} \mathbf{a}^\top \mathbf{b} d\Omega, \quad (5)$$

for any vector- or scalar-valued fields \mathbf{a} and \mathbf{b} .

When the initial condition \mathbf{u}_0 is perturbed, the linearized variations of the Lagrangian yield,

$$\delta \mathcal{L} = \delta \mathcal{J} - \int_0^T \left\{ \left[\frac{\partial \delta \mathbf{u}}{\partial t} + (\delta \mathbf{u} \cdot \nabla) \mathbf{u} + (\mathbf{u} \cdot \nabla) \delta \mathbf{u} + \nabla \delta p - \nu \nabla^2 \delta \mathbf{u}, \mathbf{u}^\dagger \right] + [\nabla \cdot \delta \mathbf{u}, p^\dagger] \right\} dt.$$

The perturbation of the cost function \mathcal{J} can be expanded as,

$$\delta \mathcal{J} = \int_0^T [\mathcal{M}^\top (\mathcal{M}(\mathbf{u}) - \mathbf{m}) - \delta(t) \lambda \nabla^2 \mathbf{u}_0, \delta \mathbf{u}] dt. \quad (6)$$

In the current study, \mathcal{J} does not depend on pressure measurements. If pressure observations are included, an additional inner-product term involving δp will be included in the variation.

Utilizing the spatial periodic boundary conditions, the inner product terms in equation (6) can be rewritten using integration by parts as,

$$\begin{aligned} & - \int_0^T \left\{ \left[\frac{\partial \delta \mathbf{u}}{\partial t} + (\delta \mathbf{u} \cdot \nabla) \mathbf{u} + (\mathbf{u} \cdot \nabla) \delta \mathbf{u} + \nabla \delta p - \nu \nabla^2 \delta \mathbf{u}, \mathbf{u}^\dagger \right] + [\nabla \cdot \delta \mathbf{u}, p^\dagger] \right\} dt \\ &= [\mathbf{u}_0^\dagger, \delta \mathbf{u}_0] - \int_0^T \left\{ \left[\frac{\partial \mathbf{u}^\dagger}{\partial(-t)} + \nabla \mathbf{u} \cdot \mathbf{u}^\dagger - (\mathbf{u} \cdot \nabla) \mathbf{u}^\dagger - \nu \nabla^2 \mathbf{u}^\dagger - \nabla p^\dagger, \delta \mathbf{u} \right] - [\nabla \cdot \mathbf{u}^\dagger, \delta p] \right\} dt. \end{aligned} \quad (7)$$

The first term on the right arises from the boundary term in time integration. Combining the two expressions, we obtain,

$$\delta \mathcal{L} = \int_0^T \left\{ - \left[\underbrace{\mathcal{N}^\dagger \mathbf{u}^\dagger}_{=0, \text{ Adjoint momentum eqns}}, \delta \mathbf{u} \right] + \left[\underbrace{\nabla \cdot \mathbf{u}^\dagger}_{=0, \text{ Adjoint continuity}}, \delta p \right] \right\} dt + [\mathbf{u}_0^\dagger, \delta \mathbf{u}_0]. \quad (8)$$

Here \mathcal{N}^\dagger is the adjoint Navier-Stokes momentum operator. The adjoint equations read

$$\frac{\partial \mathbf{u}^\dagger}{\partial(-t)} + \nabla \mathbf{u} \cdot \mathbf{u}^\dagger - (\mathbf{u} \cdot \nabla) \mathbf{u}^\dagger = \nabla p^\dagger + \nu \nabla^2 \mathbf{u}^\dagger + \mathcal{M}^\top (\mathcal{M}(\mathbf{u}) - \mathbf{m}) - \delta(t) \lambda \nabla^2 \mathbf{u}_0, \quad (9)$$

$$\nabla \cdot \mathbf{u}^\dagger = 0, \quad \mathbf{u}^\dagger|_{t=T} = \mathbf{0}.$$

The adjoint terminal condition $\mathbf{u}^\dagger|_{t=T} = \mathbf{0}$ arises from integration by parts in time to eliminate the temporal boundary term. The adjoint field may still be driven at the terminal time by the source term in the momentum equation, $\mathcal{M}^\top (\mathcal{M}(\mathbf{u}) - \mathbf{m})$.

Setting the adjoint equations renders the relation between the variation of the Lagrangian \mathcal{L} and the variation of the initial condition $\delta \mathbf{u}_0$ explicitly, and leads to the Fréchet derivative as the adjoint velocity at the initial time $t = 0$,

$$\delta \mathcal{L} = [\mathbf{u}_0^\dagger, \delta \mathbf{u}_0], \quad \nabla_{\mathbf{u}_0} \mathcal{L} = \mathbf{u}_0^\dagger. \quad (10)$$

Here the gradient symbol $\nabla_{\mathbf{u}_0}$ denotes the Fréchet derivative using the inner product (5).

B. Choice of Inner Product and the Filtered Adjoint Variables

It can be seen that the definition of the adjoint variable and the adjoint equations depend on the definition of the inner product. In general, we define a new inner product using the angle brackets,

$$\langle \mathbf{a}, \mathbf{b} \rangle = \int_{\Omega} \mathbf{a}^\top \mathcal{G}^{-1} \mathbf{b} d\Omega, \quad (11)$$

for any vector- or scalar-valued fields \mathbf{a} and \mathbf{b} . Here $\mathcal{G} \succ 0$ is a symmetric, invertible convolution operator defined as

$$(\mathcal{G}\mathbf{u})(\mathbf{x}) = \int_{\Omega} G(\mathbf{x} - \mathbf{x}') \mathbf{u}(\mathbf{x}') d\mathbf{x}', \quad (12)$$

with \mathcal{G}^{-1} the inverse operation. The relation between this new inner product and the standard inner product $[\cdot, \cdot]$ can be summarized as,

$$[\mathbf{a}, \mathbf{b}] = \int_{\Omega} \mathbf{a}^{\top} \mathbf{b} d\Omega = \int_{\Omega} \mathbf{a}^{\top} \mathcal{G}^{-1} \mathcal{G} \mathbf{b} d\Omega = \langle \mathbf{a}, \mathcal{G}\mathbf{b} \rangle = \langle \mathcal{G}\mathbf{a}, \mathbf{b} \rangle, \quad (13)$$

where symmetry of \mathcal{G} has been used in the final equality.

If G is a Dirac delta function, \mathcal{G} and \mathcal{G}^{-1} become identity maps, and the inner product $[\cdot, \cdot]$ becomes the same as $\langle \cdot, \cdot \rangle$. In the current study, the convolution is assumed to be homogeneous in space, i.e., $G(\mathbf{x} - \mathbf{x}')$ is only a function of the distance between \mathbf{x} and \mathbf{x}' . In such cases, the convolution operator \mathcal{G} and its inverse \mathcal{G}^{-1} can be more conveniently defined in the wavenumber space as,

$$\mathcal{G} = \mathcal{F}^{-1} \hat{G}(k) \mathcal{F}, \quad \mathcal{G}^{-1} = \mathcal{F}^{-1} \left(\hat{G}(k) \right)^{-1} \mathcal{F}, \quad k = |\mathbf{k}| = \sqrt{k_x^2 + k_y^2}, \quad (14)$$

where \mathcal{F} and \mathcal{F}^{-1} denote the Fourier transformation and its inverse. \hat{G} is a real-valued, positive Fourier multiplier that depends only on k . Both \mathcal{G} and \mathcal{G}^{-1} act as modewise multipliers in Fourier space. It is natural to choose \mathcal{G} as a smoothing filter. In accordance with the standard notation in the turbulence literature, we denote the filtered field by $\tilde{\mathbf{u}} = \mathcal{G}\mathbf{u}$.

The resulting Fréchet derivative of the Lagrangian to the initial condition is, similar to (10)

$$\delta\mathcal{L} = [\mathbf{u}_0^{\dagger}, \delta\mathbf{u}_0] = \langle \mathcal{G}\mathbf{u}_0^{\dagger}, \delta\mathbf{u}_0 \rangle = \langle \tilde{\mathbf{u}}_0^{\dagger}, \delta\mathbf{u}_0 \rangle, \quad \nabla_{\mathbf{u}_0}^{\mathcal{G}} \mathcal{L} = \tilde{\mathbf{u}}_0^{\dagger}. \quad (15)$$

The superscript \mathcal{G} for the gradient symbol indicates that the gradient is defined with respect to the inner product induced by \mathcal{G} in (11). It follows that the gradient is the *filtered* adjoint velocity field at the initial time. In principle, the filtered adjoint variable satisfies the corresponding filtered adjoint equations, i.e., a large-eddy-simulation (LES) form of the adjoint system. The derivation is written in Appendix A, with its further implementation and analysis left for future investigation.

C. Choice of Control Variable and Data Assimilation Framework

Employing this gradient in (15) requires that all inner products appearing in the optimization procedure be taken with respect to the modified inner product $\langle \cdot, \cdot \rangle$. In practice, this is not straightforward, as most standard optimization algorithms, e.g., Limited-memory Broyden-Fletcher-Goldfarb-Shanno (L-BFGS) method [52, 53], implicitly rely on the Euclidean inner product when computing search directions and curvature information. To avoid modifying the optimization algorithm itself, we instead introduce a transformed control variable \mathbf{s}_0 . This transformation allows the optimization to be carried out in the standard Euclidean setting, while remaining equivalent to performing the optimization with respect to the weighted inner product in the original variable \mathbf{u}_0 .

Notice that the inner product between two gradients defined by the $\nabla_{\mathbf{u}_0}^{\mathcal{G}}$ symbol is given by

$$\langle \tilde{\mathbf{u}}_0^{\dagger(1)}, \tilde{\mathbf{u}}_0^{\dagger(2)} \rangle = \langle \mathcal{G}\mathbf{u}_0^{\dagger(1)}, \mathcal{G}\mathbf{u}_0^{\dagger(2)} \rangle = \left[\mathcal{G}\mathbf{u}_0^{\dagger(1)}, \mathcal{G}^{-1}\mathcal{G}\mathbf{u}_0^{\dagger(2)} \right] = \left[\underbrace{\mathcal{G}^{1/2}\mathbf{u}_0^{\dagger(1)}}_{\mathbf{s}_0^{\dagger(1)}}, \underbrace{\mathcal{G}^{1/2}\mathbf{u}_0^{\dagger(2)}}_{\mathbf{s}_0^{\dagger(2)}} \right]. \quad (16)$$

Here $\mathcal{G}^{1/2} = \mathcal{F}^{-1} \left(\hat{\mathcal{G}}(k) \right)^{1/2} \mathcal{F}$ is half a filter. This observation naturally motivates introducing a transformed control variable \mathbf{s}_0 such that

$$\nabla_{\mathbf{s}_0} \mathcal{L} = \mathbf{s}_0^{\dagger} = \mathcal{G}^{1/2} \mathbf{u}_0^{\dagger}.$$

The \mathbf{s}_0 that satisfies this requirements is $\mathbf{s}_0 = \mathcal{G}^{-1/2} \mathbf{u}_0$, i.e., the “half-sharpened initial condition”. Since, by chain rule,

$$\nabla_{\mathbf{s}_0} \mathcal{L} = \frac{\partial \mathbf{u}_0}{\partial \mathbf{s}_0} \nabla_{\mathbf{u}_0} \mathcal{L} = \mathcal{G}^{1/2} \mathbf{u}_0^{\dagger} = \mathbf{s}_0^{\dagger}. \quad (17)$$

This perspective establishes a precise mathematical connection between the choice of control variable, the definition of inner product, adjoint filtering, and preconditioning. To help with a clear understanding, we demonstrate all these connections using a toy problem as shown in figure 1.

To illustrate how the choice of inner product and control variable alters the effective geometry of the optimization, we consider a simple two-dimensional toy problem shown in figure 1. We define the initial condition as the state vector $\mathbf{u}_0 = [u_l, u_h]^{\top}$, where the subscripts l and h denote low- and high-sensitivity directions, respectively. The cost function

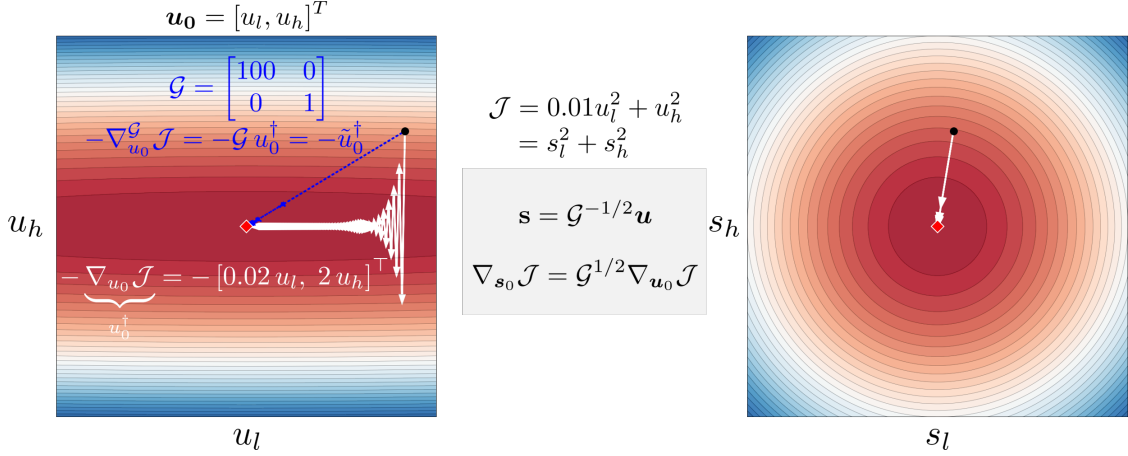


FIG. 1: A toy problem demonstration of the change of inner product and the change of control variables on the impact of optimization. Subscripts l and h mark low- and high-sensitivity parts in the initial state \mathbf{u}_0 .

is defined as $\mathcal{J} = 0.01u_l^2 + u_h^2$. In standard Euclidean space, the gradient (adjoint field) is given by $\nabla_{\mathbf{u}_0} \mathcal{J} = [0.02u_l, 2u_h]^\top$. The resulting steepest descent direction is heavily biased toward the high-sensitivity component, yielding a poorly conditioned, zig-zag path on the stretched level sets (left panel). As demonstrated in Section II B, the preconditioning can be viewed as a change of inner product. Choosing the filter $\mathcal{G} = \text{diag}(100, 1)$ compensates for the imbalance in sensitivity, producing a direct descent direction ($\nabla_{\mathbf{u}_0}^{\mathcal{G}} \mathcal{J}$, marked by the blue dashed arrow) in the original physical space. Equivalently, this can be framed as a change of control variable $\mathbf{s}_0 = \mathcal{G}^{-1/2} \mathbf{u}_0$. This transformation maps the distorted physical landscape to a latent space \mathbf{s}_0 (right panel) where the cost function becomes better conditioned in the new variable, i.e., $\mathcal{J} = s_l^2 + s_h^2$. Applying the chain rule, the gradient in the transformed variable is $\nabla_{\mathbf{s}_0} \mathcal{J} = \mathcal{G}^{1/2} \nabla_{\mathbf{u}_0} \mathcal{J} = [2s_l, 2s_h]^\top$, which yields a perfectly conditioned path to the minimizer and therefore requires fewer steps and less time to converge, while achieving higher accuracy.

We illustrate this framework for the data assimilation of two-dimensional turbulence in figure 2. We assume that the observations consist of velocity measurements taken at spatial locations $\{\mathbf{x}_i^m\}_{i=1}^{N_{\text{obs}}}$ and discrete times $\{t_j^m\}_{j=1}^{N_t}$. This corresponds to a measurement operator \mathcal{M} composed of Dirac delta functions in space and time, mapping the model state to the observed velocity samples. On the left side of figure 2, we introduce the spectral preconditioner by redefining the control variable as $\mathbf{s}_0 = \mathcal{G}^{-1/2} \mathbf{u}_0$. If \mathcal{G} is interpreted as a

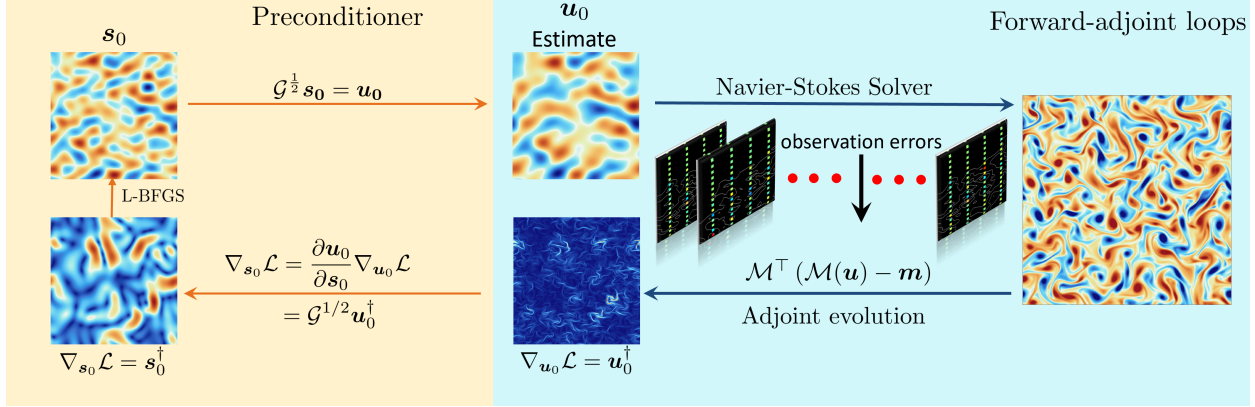


FIG. 2: Data assimilation framework with preconditioner \mathcal{G} .

smoothing filter, then the adjoint gradient in the transformed space, \mathbf{s}_0^\dagger , corresponds to a filtered version of the physical adjoint \mathbf{u}_0^\dagger , while the mapping from \mathbf{s}_0 back to \mathbf{u}_0 introduces an additional filtering operation. Consequently, during each optimization step, the update direction applied to the physical initial condition effectively involves two operations of $\mathcal{G}^{1/2}$, resulting in a scale-selective damping of high-wavenumber components in the gradient. The minimization of the cost functional \mathcal{J} is carried out using the L-BFGS algorithm [52]. At iteration k , the control variable is updated according to

$$\mathbf{s}_0^{(k+1)} \leftarrow \text{L-BFGS}(\mathbf{s}_0^{(k)}, \mathbf{s}_0^{\dagger(k)}), \quad k = 1, \dots, N.$$

after which the physical initial condition \mathbf{u}_0 is recovered through the $\mathcal{G}^{1/2}$ transformation.

This formulation is closely related to latent-space data assimilation [39] and precursor-simulation strategies, in which the optimization is performed in a transformed representation of the state variables. In contrast to approaches that rely on extended backward integration windows to enhance reconstruction fidelity, the present method achieves scale-aware regularization directly through an explicit metric transformation in control space.

III. RESULTS

The flow field considered is the two-dimensional decaying homogeneous isotropic turbulence (HIT), with an initial condition generated with a given energy spectrum and random phase. Numerical solutions are obtained via a fractional step method [54]: an intermediate velocity field is computed by ignoring the continuity equation and pressure gradient in

Domain size		Grid points		Temporal resolution		Observations		Parameters	
L_x	L_y	N_x	N_y	Δt	T	ΔI	Δt_m	Re	N
2π	2π	512	512	0.002	2.0	8	0.1	1000	100

TABLE I: Simulation and data-assimilation parameters for the 2D decaying HIT case.

each time step, followed by solving the pressure Poisson equation and performing a projection of velocities onto a divergence-free space using the pressure gradient as the minimum correction. Temporal integration employs a second-order Adams-Bashforth scheme for the explicit advection and Crank-Nicolson for diffusion. Diffusion inversion and solving the pressure Poisson equation utilize modified wavenumbers in Fourier space, mirroring a central difference scheme.

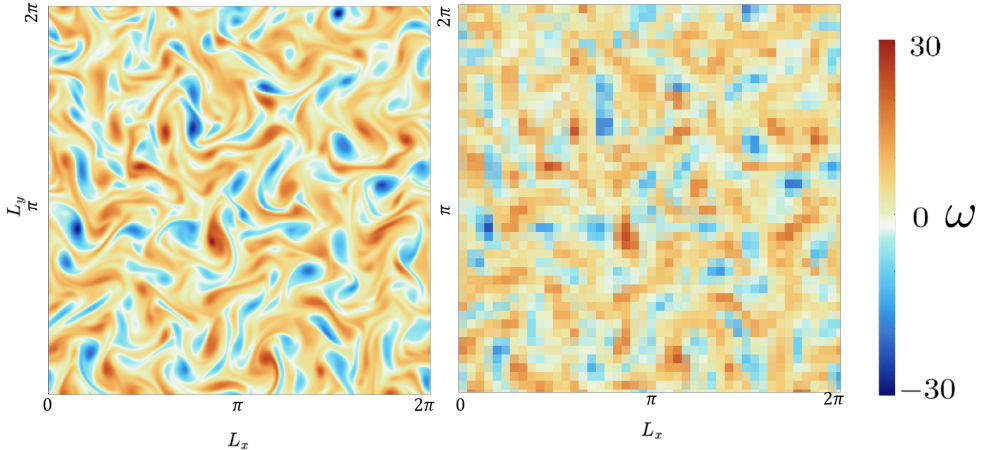


FIG. 3: Illustration of the underlying grid resolution in a two-dimensional periodic domain of size $x = y = 2\pi$. (a): a representative patch of the full 512×512 grid. (b): the observed grid obtained by downsampling with a grid gap of $\Delta I = 8$, corresponding to an effective 64×64 resolution.

The adjoint equations are derived through a summation-by-parts procedure, which ensures the gradient computations (10) and (15) are satisfied to machine precision. The simulation is performed on a double periodic domain $\Omega = [0, 2\pi]^2$; relevant parameters are summarized in Table I. The initial condition for the two-dimensional decaying turbulence is generated from a prescribed isotropic energy spectrum of the form $E_{0,r}(k) = C k^4 \exp\left[-\left(\frac{k}{k_0}\right)^2\right]$,

where k_0 denotes the characteristic energy-containing wavenumber, and C is a normalization constant chosen to achieve the desired initial kinetic energy. Random phases are assigned in Fourier space, and the velocity field is projected onto a divergence-free space to ensure incompressibility before transforming back to physical space.

For a given velocity field $\mathbf{u} = (u, v)$ defined on a two-dimensional periodic domain, the one-dimensional (isotropic) energy spectrum $E(k)$ is computed from its two-dimensional Fourier transform. We first form the spectral kinetic-energy density and obtain the isotropic energy spectrum by summing over concentric shells of constant wavenumber magnitude,

$$E(k) = \sum_{k \leq |\mathbf{k}| < k + \Delta k} \underbrace{\frac{1}{2} |\hat{\mathbf{u}}(\mathbf{k})|^2}_{\mathcal{E}(\mathbf{k})}, \quad (18)$$

where $k = |\mathbf{k}|$ and Δk denotes the shell width in wavenumber space.

A representative flow field at time $t = 0.2$ is shown in terms of vorticity contours in Fig. 3, which also illustrates the effect of the chosen observation gap $\Delta I = 8$.

A. Examples of Control-Variable Choices

From equation (11), the choice of control variable \mathbf{s}_0 directly determines the form of the convolution operator \mathcal{G} . For instance, when the vorticity field ω is used as the control variable, the forward velocity field in Fourier space is recovered through the Biot-Savart relation,

$$\hat{\mathbf{u}}(\mathbf{k}) = i \frac{\mathbf{k}^\perp}{k^2} \hat{\omega}(\mathbf{k}), \quad \mathbf{k}^\perp = (-k_y, k_x),$$

which implies that the kinetic energy and enstrophy spectra are connected by $E_\omega(\mathbf{k}) = k^2 E_u(\mathbf{k})$. Hence, the natural inner product between two vorticity fields ω_1 and ω_2 corresponds to the \mathcal{G} -inner product on the velocity fields \mathbf{u}_1 and \mathbf{u}_2 with Fourier multiplier $\hat{G}(k) = 1/k^2$,

$$[\omega_1, \omega_2] = \int_{\mathbf{k}} \hat{\omega}_1^*(\mathbf{k}) \hat{\omega}_2(\mathbf{k}) d\mathbf{k} = \int_{\mathbf{k}} k^2 \hat{\mathbf{u}}_1^*(\mathbf{k}) \hat{\mathbf{u}}_2(\mathbf{k}) d\mathbf{k} = \langle \mathbf{u}_1, \mathbf{u}_2 \rangle_{\hat{G}=1/k^2}. \quad (19)$$

Similarly, the effect of using streamfunction as the control vector for the data assimilation can be assessed via $\hat{\mathbf{u}}(\mathbf{k}) = i \mathbf{k}^\perp \hat{\psi}(\mathbf{k})$. The inner product between two streamfunctions then becomes an integral of $k^{-2} \hat{\mathbf{u}}_1^*(k) \hat{\mathbf{u}}_2(k)$ in the Fourier space, showing that energy of the streamfunction scales with kinetic energy by k^{-2} , i.e,

$$[\psi_1, \psi_2] = \langle \mathbf{u}_1, \mathbf{u}_2 \rangle_{\hat{G}=k^{-2}}. \quad (20)$$

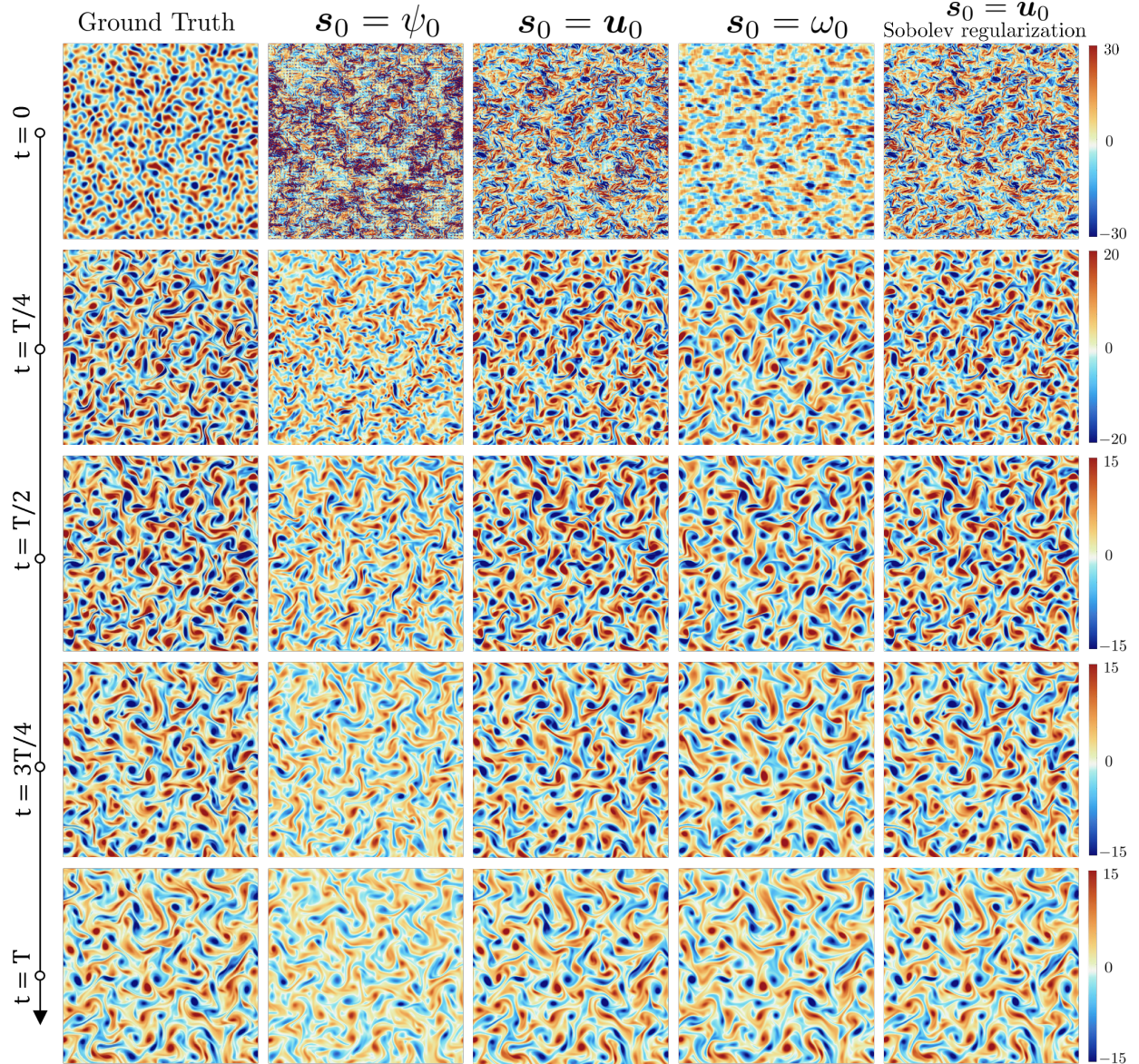


FIG. 4: Snapshots of true fields and reconstructed fields from $t=0$ to $t = T$.

To assess the impact of control-variable choice on reconstruction accuracy, we perform data assimilation using four different control vectors: velocity \mathbf{u}_0 , vorticity ω_0 , streamfunction ψ_0 , and velocity with Sobolev regularization $\lambda = 1 \times 10^{-3}$. The value of λ is chosen by running a short optimization (a few L-BFGS iterations) for several candidate values and selecting the one that yields the lowest objective before performing the full assimilation. Figure 4 presents a time sequence of two-dimensional turbulence fields, in terms of vorticity contour, at five representative instants: $t = 0, T/4, T/2, 3T/4$, and T (rows). Each column compares the ground-truth field to model reconstructions using the control vector \mathbf{s}_0 being

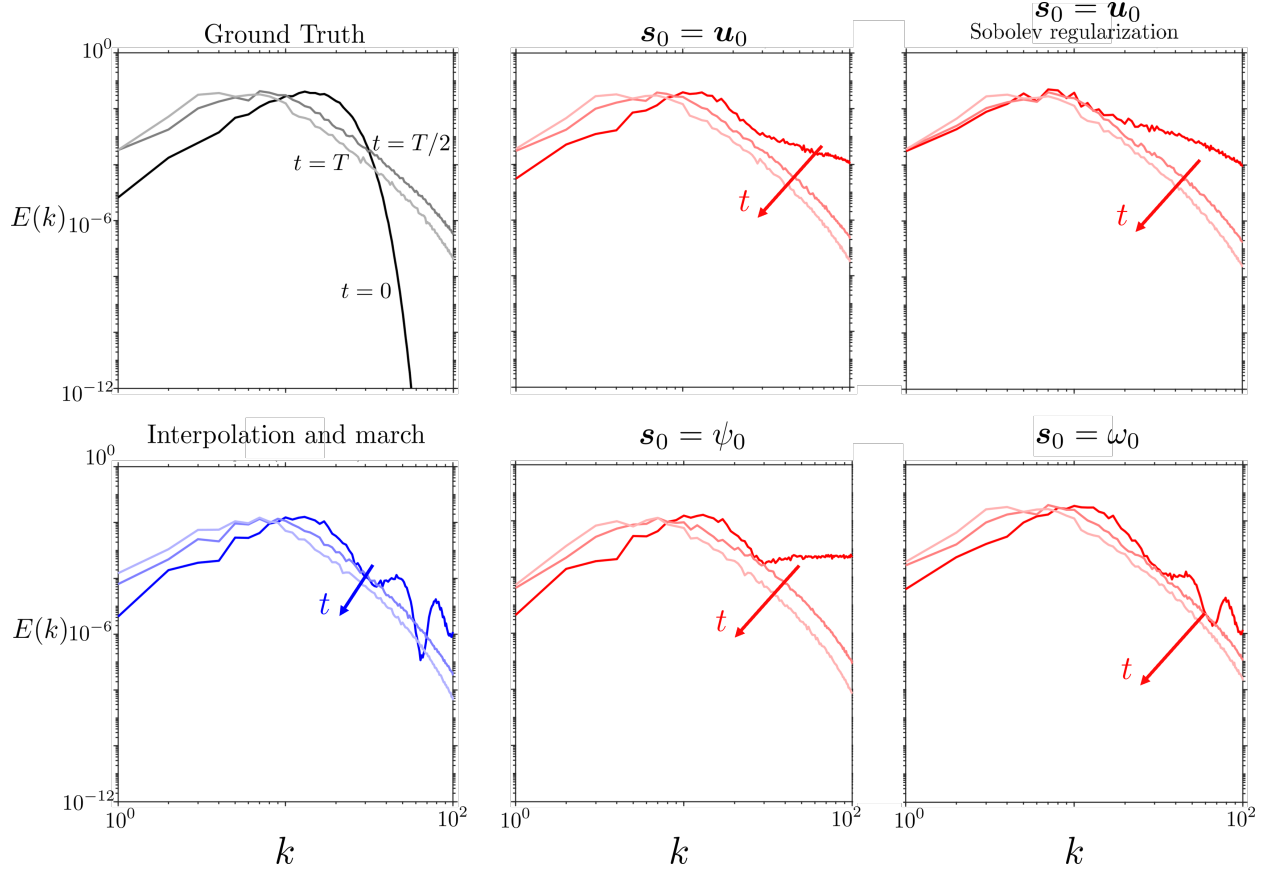


FIG. 5: Energy spectra $E(k)$ under different choice of control variables \mathbf{s}_0 . Each subplot corresponds to a specific control strategy or regularization method. For each color group, the curves represent the temporal evolution of the energy spectrum, with lighter shades indicating later times ($t = 0 \rightarrow T$).

(i) velocity components $\mathbf{s}_0 = \mathbf{u}_0$, (ii) vorticity $\mathbf{s}_0 = \omega_0$, (iii) streamfunction $\mathbf{s}_0 = \psi_0$, and (iv) a Sobolev-regularized case with $\mathbf{s}_0 = \mathbf{u}_0$. All panels share a consistent colormap, with colorbars normalized per row to facilitate temporal comparison. Visually, the reconstructions exhibit strong phase fidelity across time, with large-scale structures accurately positioned. Reconstructions based on \mathbf{u}_0 most closely match the ground truth. When ω_0 is used as the control vector, the method exhibits heightened sensitivity to small-scale gradients, resulting in well-resolved fine-scale structures but noticeable discrepancies at low wavenumbers, manifested as mild smoothing and reduced filament sharpness. In contrast, using ψ_0 as the control vector leads to the emergence of spurious fine-scale features, reflecting the reduced sensitivity of the optimization to such structures. The Sobolev diagnostic indicates that the method broadly preserves multiscale regularity, though the finest-scale textures are

somewhat attenuated.

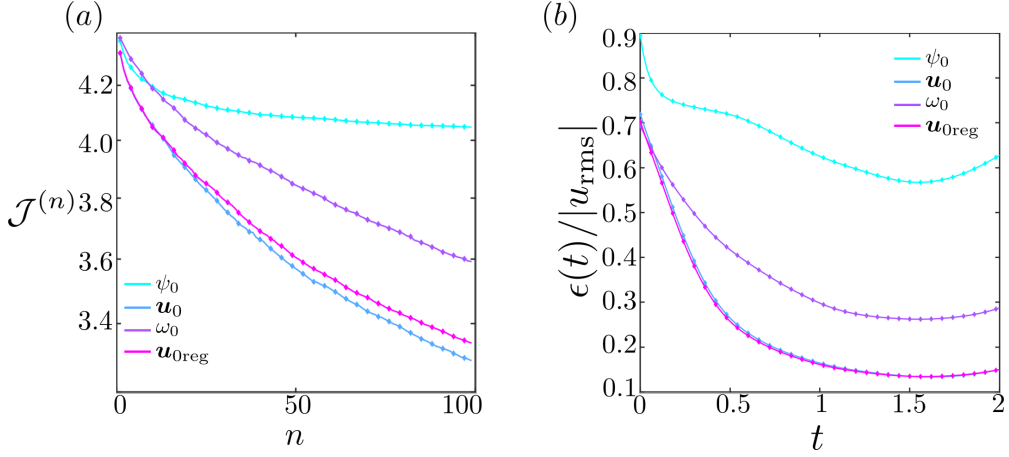


FIG. 6: (a) Convergence histories of the objective function $\mathcal{J}^{(n)}$ over L-BFGS iterations for different control vectors. (b) Time evolution of normalized reconstruction error $\epsilon(t)$ for different control vectors and regularization choices.

Figure 5 summarizes the performance of the data assimilation procedure across control variables. The energy spectra $E(k)$ for the evolution of initial fields reconstructed using different control variables are reported. Blue curves correspond to the initial interpolated state and its evolution in time. Gray curves represent ground-truth snapshots, while red curve families illustrate the evolution of reconstructions over time using different control variables \mathbf{s}_0 . At the initial time $t = 0$, the reconstructions using the vorticity ($\mathbf{s}_0 = \omega_0$) perform comparably to the interpolation, while all other reconstructions show different levels of mismatch, especially in the high wavenumber region. This trend reflects the intrinsic scale-dependent sensitivity of the adjoint dynamics: backward integration amplifies small-scale components more strongly, causing the optimization to favor high-wavenumber corrections unless appropriately regularized. As the flow evolves in time, all reconstructions progressively improve in terms of accuracy. In addition, the Sobolev-regularized optimization recovers the wrong low-wavenumber energy, while the closest recovery is the one using velocity \mathbf{u}_0 as the control vector.

Overall quantification of reconstruction qualities is shown in figure 6. The left panel plots the objective functional $\mathcal{J}^{(n)}$ versus iteration count n for various control configurations. Using velocity control vector $\mathbf{s}_0 = \mathbf{u}_0$ without Sobolev regularization (blue) exhibits the fastest descent and lowest minimum, indicating superior optimization efficacy. With

regularization (purple), the results are less accurate, although still better than using other control variables. Results with $s_0 = \omega_0$ (light purple) descend more slowly, while $s_0 = \psi_0$ (cyan) converges the slowest and reaches a plateau after a few iterations—consistent with its spectral difficulty. The right panel presents the normalized root-mean-square error as a function of time and exhibits the same qualitative trends. In all cases, the error decreases in time, reflecting the increasing influence of later observations relative to earlier ones. This behavior is a direct consequence of adjoint-field growth and will be examined in more detail in subsequent sections.

For a final sanity check, we compare the data assimilation using preconditioner with the Fourier multiplier $\hat{G}(k) = 1/k^2$ and compare with the result using the vorticity ω_0 as the control variable. The results are shown in figure 7. The left panel presents the reconstruction obtained from vorticity-based control, while the right panel shows the result produced by applying spectral preconditioning to the velocity field using k -scaled modes. After $N = 100$ optimization iterations, the two reconstructed initial conditions are identical, indicating the equivalence of the two approaches.

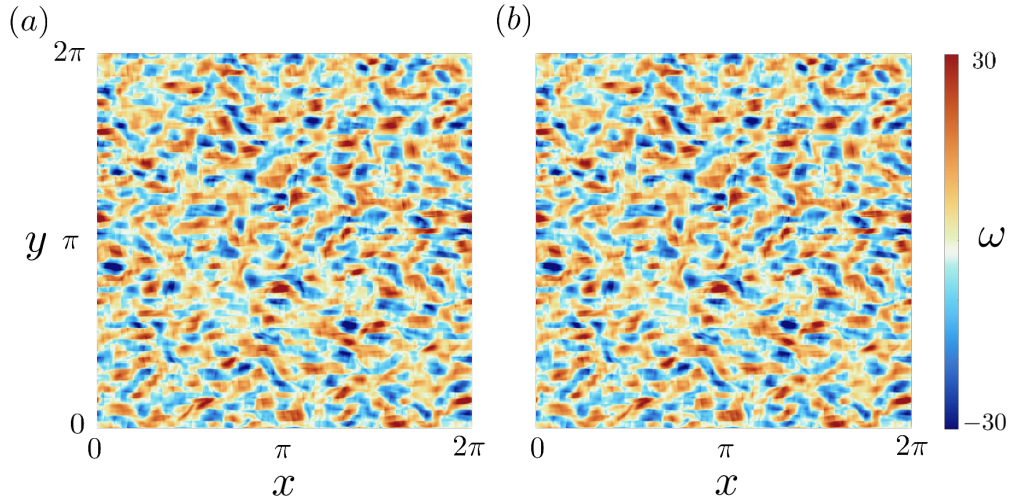


FIG. 7: Comparison of initial condition reconstruction as a validation case. (a) Direct reconstruction using vorticity ω_0 as control variable. (b) Reconstruction with preconditioner with Fourier multiplier $\hat{G} = 1/k^2$.

B. Construction of Spectral Filter as Preconditioner

Motivated by this observed equivalence, we now formalize the construction of a spectral filter as a preconditioner, within which the choice of control variable, including vorticity, streamfunction, velocity, or even intermediate representations, can be treated in a unified manner. We are particularly interested in two types of preconditioner here,

$$\widehat{G}_p(k; \alpha) = k^{-2\alpha}, \text{ and } \widehat{G}_e(k; \beta) = \exp(-\nu\beta k^2),$$

with subscripts p and e indicating power law and exponential. Here we exclude the zero wavenumber mode by setting $\widehat{G}(0) = 1$ in the code to avoid singularities. In Fourier space, the scaled control variables for the two scenarios are respectively

$$\widehat{\mathbf{s}}_p(k) = \widehat{G}_p^{-1/2}(k) \widehat{\mathbf{u}}_0(k) = k^\alpha \widehat{\mathbf{u}}_0(k), \quad \widehat{\mathbf{s}}_e(k) = \widehat{G}_e^{-1/2}(k) \widehat{\mathbf{u}}_0(k) = \exp\left(\frac{1}{2}\nu\beta k^2\right) \widehat{\mathbf{u}}_0(k).$$

These control variables can be physically interpreted. If we regard the vorticity and stream function as the order 1 and -1 derivatives of a two-dimensional incompressible velocity field, the algebraic family defines the fractional derivatives of \mathbf{u}_0 . Correspondingly, \mathbf{u}_0 is a fractional integral of \mathbf{s}_0 for non-integer α .

For the preconditioner in the exponential-family, the transformed control variable uses a heat-kernel-type factor that damps high k when $\beta > 0$. Equivalently, the mapping from the latent control \mathbf{s}_0 back to the physical initial condition \mathbf{u}_0 is

$$\widehat{\mathbf{u}}_0(k) = \exp\left(-\frac{1}{2}\nu\beta k^2\right) \widehat{\mathbf{s}}_e(k). \quad (21)$$

Since $\exp(\tau\Delta)$ has Fourier symbol $\exp(-\tau k^2)$, the operator $\exp(-\frac{1}{2}\nu\beta k^2)$ in (21) corresponds to a diffusive (smoothing) step in the $\mathbf{s}_0 \mapsto \mathbf{u}_0$ mapping, with the diffusivity ν and diffusion time $\beta/2$. when $\beta > 0$: the velocity is smoothed from the control variable \mathbf{s}_0 by $\mathcal{G}_e^{1/2}$, as in figure 2. In contrast, $\beta < 0$ yields a sharpening in the $\mathbf{s}_0 \mapsto \mathbf{u}_0$ mapping that further amplifies high-wavenumber modes, which is not preferable here.

In addition, these spectral weighting choices have clear implications for how different spectral bands are emphasized in the control formulation. In two-dimensional decaying homogeneous isotropic turbulence, the energy spectrum exhibits distinct power-law ranges associated with the inverse energy transfer and the forward enstrophy cascade, with an exponential decay in the viscous range. These spectral characteristics motivate the choice of scale-dependent preconditioners in the present work.

C. Results with Algebraic Spectral Preconditioners

We first present the results of the algebraic family

$$\hat{G}_p(k) = k^{-2\alpha}, \quad \hat{s}_p(k) = k^\alpha \hat{u}_0(k).$$

We scan $\alpha \in [-2, 2]$ with step $\Delta\alpha = 0.1$; for each α , the optimization starts from the same initial guess and is run with identical L-BFGS settings.

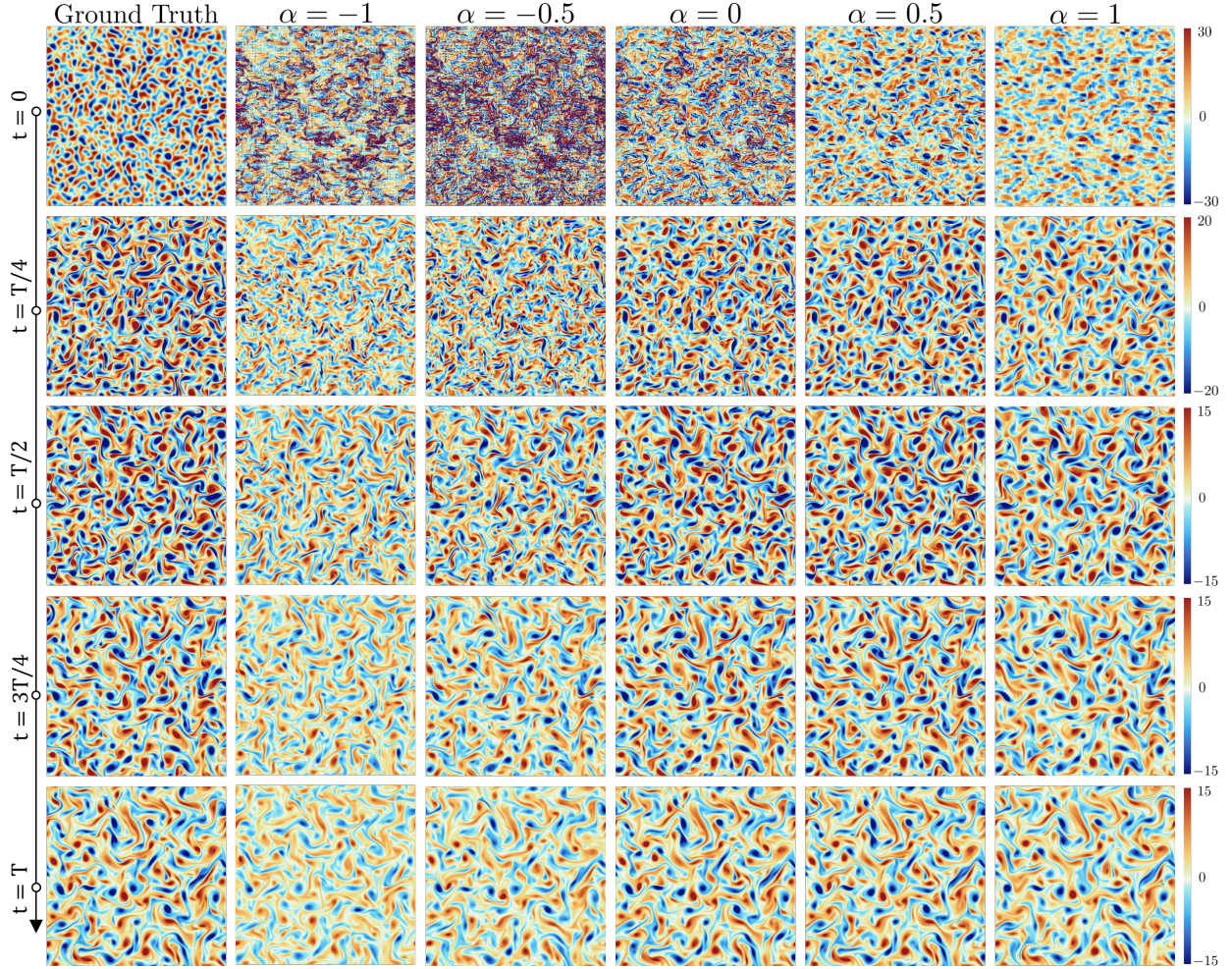


FIG. 8: Snapshots of the true velocity magnitude and the reconstructed velocity fields at $t = \{0, 0.5, 1, 1.5, 2\}$ for several values of the algebraic preconditioner $\hat{G}_p(k) = k^{-2\alpha}$.

Figure 8 illustrates the reconstruction quality for different values of the spectral exponent α . For moderate $|\alpha|$, the reconstructed vorticity fields capture both large-scale coherence and small-scale enstrophy with minimal spurious oscillations. As α approaches ± 1 , the behavior becomes consistent with vorticity-like ($\alpha = +1$) and streamfunction-like ($\alpha = -1$)

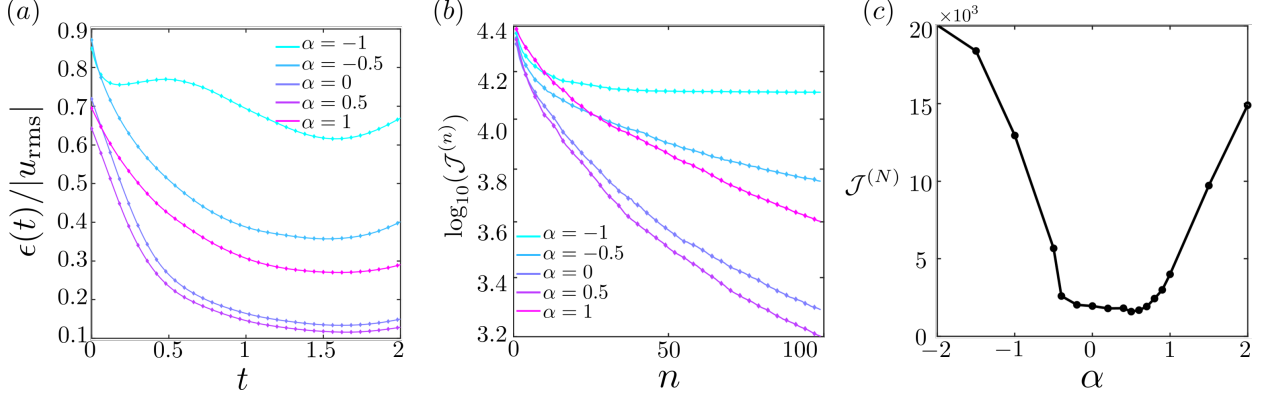


FIG. 9: (a) Reconstruction error of the velocity field, $\epsilon(t)$, normalized by the instantaneous root-mean-square (RMS) magnitude of the ground-truth velocity fluctuations, $u_{\text{rms}}(t)$, as a function of time t . (b) Convergence histories of the objective function $\mathcal{J}^{(n)}$ over L-BFGS iterations for different α , plotted on a logarithmic scale. (c) Final objective value $\mathcal{J}^{(N)}$ versus the spectral preconditioning exponent α for the family $\hat{G}_p(k) = k^{-2\alpha}$.

control metrics: positive α resolves finer structures but increases stiffness, whereas negative α yields smoother initial fields that fit large scales well but tend to under-represent small-scale vortices.

The corresponding optimization behavior is shown in figure 9. The reconstruction error $\epsilon(t) = \|\mathbf{u} - \mathbf{u}_r\|$ is shown in panel (a), with the convergence history during $N = 100$ L-BFGS iterations shown in panel (b), for selected values of α . In all cases, the error decreases in forward time. This trend can be attributed to two mechanisms. First, two-dimensional decaying homogeneous isotropic turbulence exhibits progressive spectral smoothing due to viscous dissipation, which reduces discrepancies as the flow evolves. Second, the adjoint field grows exponentially in backward time, so that measurements taken closer to the final time exert a disproportionately larger influence on the gradient at $t = 0$. As a result, the optimization procedure tends to prioritize matching later-time observations, leading to smaller reconstruction errors near the end of the assimilation window. Panel (c) shows the final objective value $\mathcal{J}^{(N)}$ as a function of α . Note that \mathcal{J} decreases as α moves from negative to mildly positive values, reaching its minimum near $\alpha \approx 0.5$. This choice slightly favors enstrophy-bearing small scales, strengthening high- k corrections enough to compensate for under-resolved gradients induced by coarse observations, while keeping the adjoint dynamics and the L-BFGS iterations numerically stable. For excessively large $|\alpha|$, the L-BFGS step

size often collapses, and the optimization terminates early, indicating severe ill-conditioning. Overall, the observed U-shaped dependence of $\mathcal{J}^{(N)}$ on α quantifies the trade-off introduced by spectral preconditioning: small $|\alpha|$ provides the best balance between stability and accuracy, while very large $|\alpha|$ either over-amplifies high- k sensitivity or over-damps small-scale corrections.

D. Results with Exponential (Diffusion-Like) Spectral Preconditioner

For the exponential family, we systematically scan β over the interval $[-0.1, 0.8]$ with a uniform step size with $\Delta\beta = 0.05$, starting from the same initial guess and using identical L-BFGS settings as in the algebraic family.

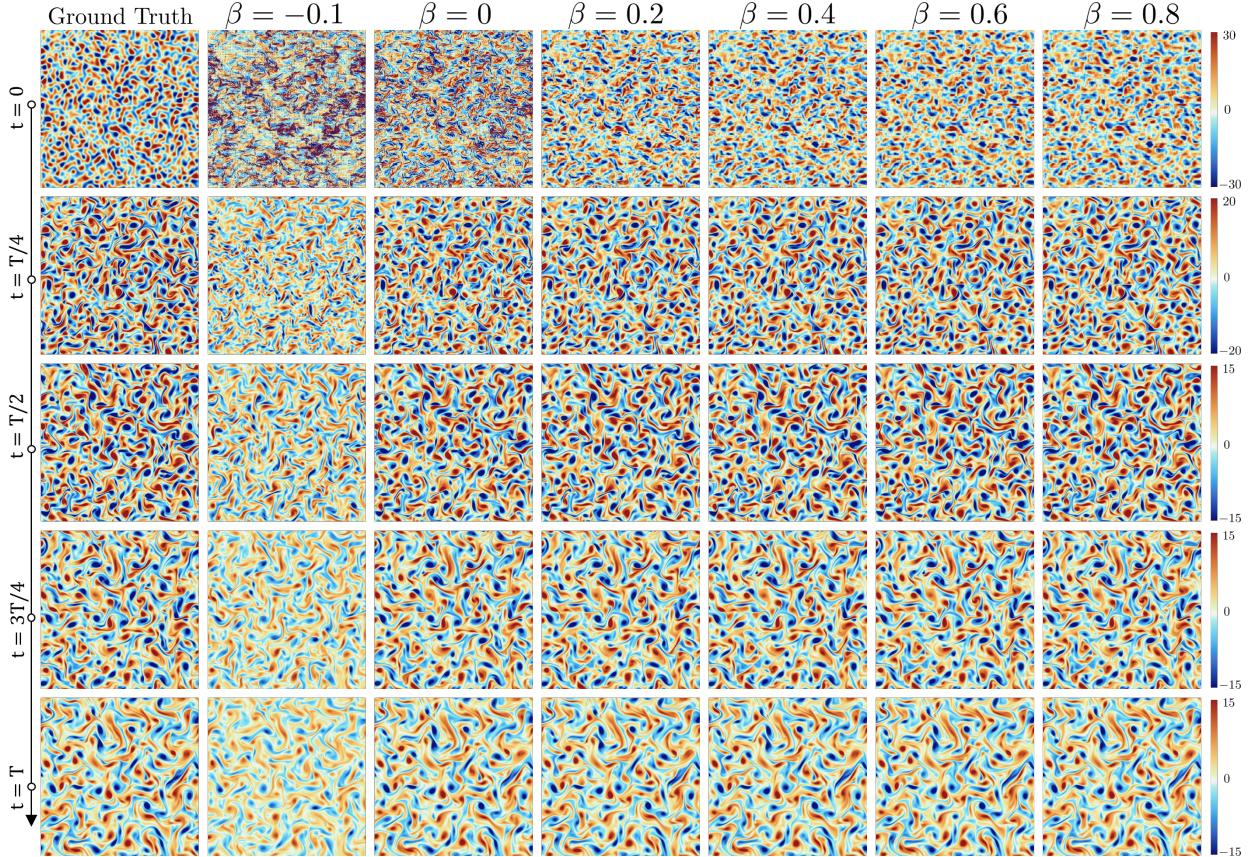


FIG. 10: Snapshots of the true velocity magnitude and the reconstructed velocity fields at $t = \{0, 0.5, 1, 1.5, 2\}$ for several values of the diffusion time parameter β in the preconditioner \mathcal{G}_e .

Figure 10 illustrates the effect of β on the reconstruction quality, with $\widehat{G}_e(k) = \exp(-\nu\beta k^2)$.

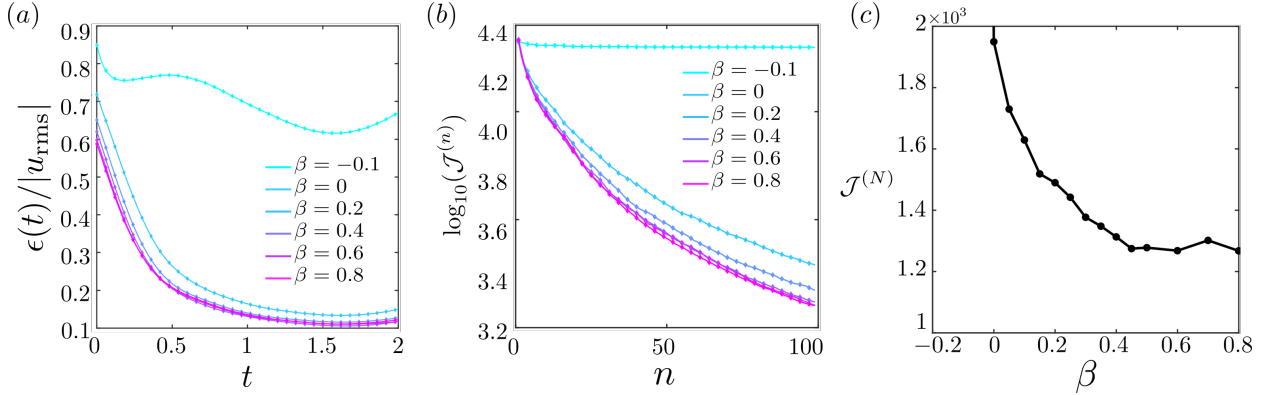


FIG. 11: (a) Evolution of the error in velocity prediction, normalized by the Root-Mean-Square (RMS) value, as a function of time t after 100 L-BFGS iterations. (b) Convergence histories of the objective function $\mathcal{J}^{(n)}$ over L-BFGS iterations for different β , plotted on a logarithmic scale. (c) Final objective value $\mathcal{J}^{(N)}$ versus β for the family $\hat{G}_e(k) = \exp(-\nu\beta k^2)$.

For very small β , $\hat{G}_e(k) \approx 1$, and the performance essentially coincides with that using the vanilla adjoint. As β increases to moderate positive values, the reconstructed initial fields become smoother and more physically plausible: small-scale noise in the adjoint gradient is efficiently damped while large-scale structures are preserved.

The corresponding optimization behavior is shown in figure 11. The temporal evolution of the velocity mismatch exhibits trends similar to those observed with the algebraic preconditioner, as illustrated in panel (a). However, the exponential family yields the largest improvement in the reconstruction of the initial condition. Compared with the standard (unweighted) adjoint formulation, it achieves up to 35% reduction in the initial-condition error. In panel (b), it is clear that using a negative β leads to stagnation of the optimization, with the cost function failing to decrease after a few iterations. The final loss in panel (c) decreases as β increases to moderate positive values; the best overall performance is obtained at an intermediate value, around $\beta \approx 0.8$, where the preconditioner achieves a favorable balance between selective high- k damping and retention of dynamically relevant large-scale structure. For very large values of β (e.g., $\beta \approx 1.0$, which lies outside the range shown in the figure), the gradient becomes excessively smoothed, effectively removing almost all high-wavenumber corrections. As a result, the optimization loses its ability to recover fine-scale structures. In this regime, the problem also becomes numerically stiff, and

the L-BFGS step size may collapse, causing the optimization to terminate prematurely and yielding a larger final loss. For sufficiently large negative β , the exponential factor no longer damps high-wavenumber modes but instead amplifies them. This amplification destabilizes the adjoint update, and the optimization typically diverges or suffers numerical blow-up.

Comparing the two families, the algebraic preconditioner $\widehat{G}(k) = k^{-2\alpha}$ provides a gentle spectral tilt that continuously interpolates between control-variable metrics, whereas the exponential preconditioner acts as a diffusion operator that sharply damps noise near the grid scale. In our 2D decaying HIT test case, both families exhibit an optimal intermediate parameter range: the algebraic family achieves its best performance around $\alpha \approx 0.5$, while the exponential family attains its most accurate reconstructions and fastest convergence near $\beta \approx 0.8$. Overall, the exponential preconditioner is less sensitive to high-wavenumber contamination and delivers more robust smoothing and consistently better performance than the algebraic family across the range of parameters tested.

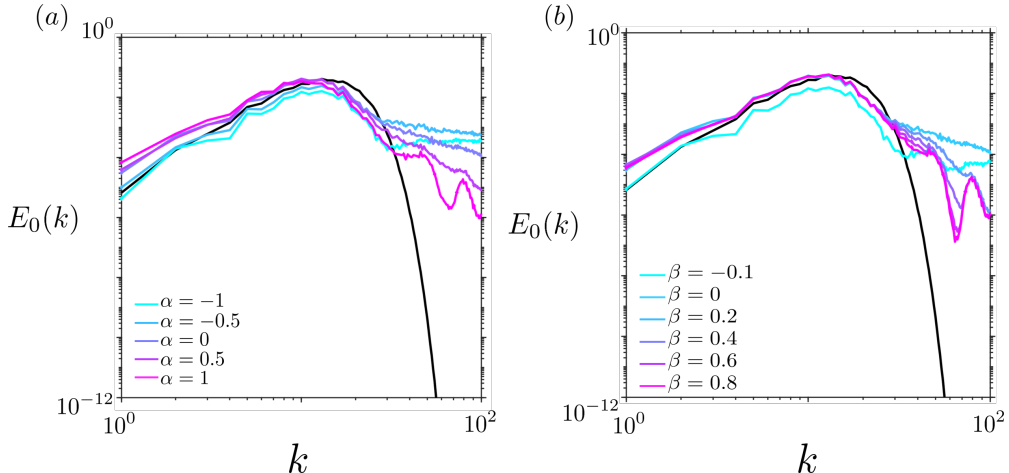


FIG. 12: Energy spectrum $E(k)$ of the reconstructed initial condition at $t = 0$ for different spectral preconditioners, compared with the ground-truth spectrum. (a) algebraic family $\widehat{G}(k) = k^{-2\alpha}$: curves for several α values. (b) Exponential family $\widehat{G}_e(k) = \exp(-\nu\beta k^2)$: curves for several β values. Both axes are on logarithmic scales; the ground truth is shown for reference.

To visualize the effect of these two families of preconditioners on the quality of data assimilation across wavenumbers, figure 12 quantifies this behavior in spectral space by comparing the energy spectrum $E(k)$ of the reconstructed initial condition at $t = 0$ with the ground-truth spectrum for selected values of α and β . For the algebraic family (panel a), the

curve corresponding to $\alpha \approx 0.5$ tracks the ground truth most closely across wavenumbers. Smaller $|\alpha|$ tends to leave excess energy at high k due to under-damped gradient noise, whereas larger α suppresses high- k content and yields a spectrum that exceeds the ground truth at small scales. For the exponential family (panel b), $\beta \approx 0.8$ provides the best overall spectral match: the reconstructed spectrum aligns with the ground truth across the resolved range, while smaller β again produces excess energy at high k . The case $\beta = 0.6$ behaves nearly identically to $\beta = 0.8$, consistent with earlier diagnostics; both values provide sufficient high-wavenumber damping, and their spectra differ only slightly near the grid scale. Comparison with the reconstruction snapshots further shows that the fidelity of the high- k portion of $E(k)$ largely determines the qualitative quality of the recovered initial field. Across the tested parameter ranges, the exponential family consistently delivers cleaner high- k smoothing than the algebraic family, explaining why its reconstructions remain more stable and visually accurate over a broader range of parameter choices.

These results demonstrate that the choice of \widehat{G} provides a systematic way to tune the spectral balance of adjoint sensitivity and improve the conditioning of the inverse problem. Especially, the diffusion kernel with $\beta \approx 0.8$ yields the lowest cost functional among all cases. This observation suggests that incorporating a diffusion-dominated process—or an analogous smoothing dynamics—as a precursor simulation within the data assimilation procedure can significantly enhance both accuracy and numerical stability.

IV. STATISTICAL ANALYSIS OF ADJOINT SENSITIVITY

To better understand the properties of the gradient information used in the optimization and understand the spatiotemporal behavior of the optimized fields, we analyze the spatiotemporal evolution of the adjoint fields using an ensemble-based impulse response method. We consider a terminal point perturbation in the u component at $t = T$ and propagate it backward using the adjoint equations, i.e., evaluating the adjoint Green's function. Similar to our previous research [18, 19], this adjoint Green's functions effectively defines the spatiotemporal domain of dependence for a later measurement (in this case, the u component at a single point). Since the adjoint dynamics depend on the underlying forward realization of homogeneous isotropic turbulence, we generate an ensemble of forward fields sharing the same initial energy spectrum $E_{0,r}$, but with random phases, and evolve these

fields forward in time. Each realization is evolved forward in time, and the corresponding adjoint field is then integrated backward from the same terminal measurement kernel. This procedure yields an ensemble of adjoint fields, which enables statistical characterization of their scale-dependent structures.

Figure 13 visualizes the adjoint fields, in terms of the magnitude of adjoint velocity fields, $|\mathbf{u}^\dagger|$. The adjoint fields characterize the region at an earlier time t that influences the observation at the terminal time $t = T$. The top row of figure 13 displays a single realization from the ensemble. The adjoint field is characterized by fine-scale, filamentary structures distributed throughout the domain, reflecting the chaotic nature of the flow, in which infinitesimal perturbations undergo exponential amplification when evolved backward in time. This behavior is closely connected to the Lyapunov spectrum of the system, as discussed in Wang *et al.* [19], Nikitin [31]. The filament thickness in the adjoint vorticity field is extremely small, consistent with the Kolmogorov length scale governing the smallest dynamically active structures in the flow [55]. In contrast, the bottom row shows the ensemble-averaged adjoint fields, using 3000 samples. Here, the chaotic fluctuations cancel out, revealing a smooth core domain of dependence. This distinct difference suggests that while the instantaneous sensitivity is dominated by chaotic noise, the underlying physical connection between the terminal observation and the initial state remains deterministic but is obscured by small-scale instabilities — a typical backward chaotic behavior [50].

To quantify the growth and scale dependence of adjoint energy, we analyze ensemble- and shell-averaged statistics in Fourier space. We therefore introduce the ensemble average, denoted by $\overline{(\cdot)}$, and use the backward time $\tau = T - t$ to analyze the adjoint fields. For each turbulence realization, the adjoint field is transformed to Fourier space, and its energy is accumulated over concentric wavenumber shells, yielding a shell-averaged adjoint energy as a function of the wavenumber magnitude k . Based on this construction, we consider two shell-averaged adjoint energy measures in wavenumber space. The first is the energy of the ensemble-mean adjoint field, $\|\overline{\hat{\mathbf{u}}^\dagger}(k, \tau)\|^2$, obtained by first averaging the adjoint Fourier coefficients across realizations and then computing the shell energy. The second is the ensemble-averaged adjoint energy, $\|\hat{\mathbf{u}}^\dagger(k, \tau)\|^2$, obtained by averaging the shell-wise energy over realizations. The former quantifies the large-scale structures, the reproducible component of adjoint sensitivity at scale k , whereas the latter represents the total adjoint energy, including small-scale structure fluctuations.

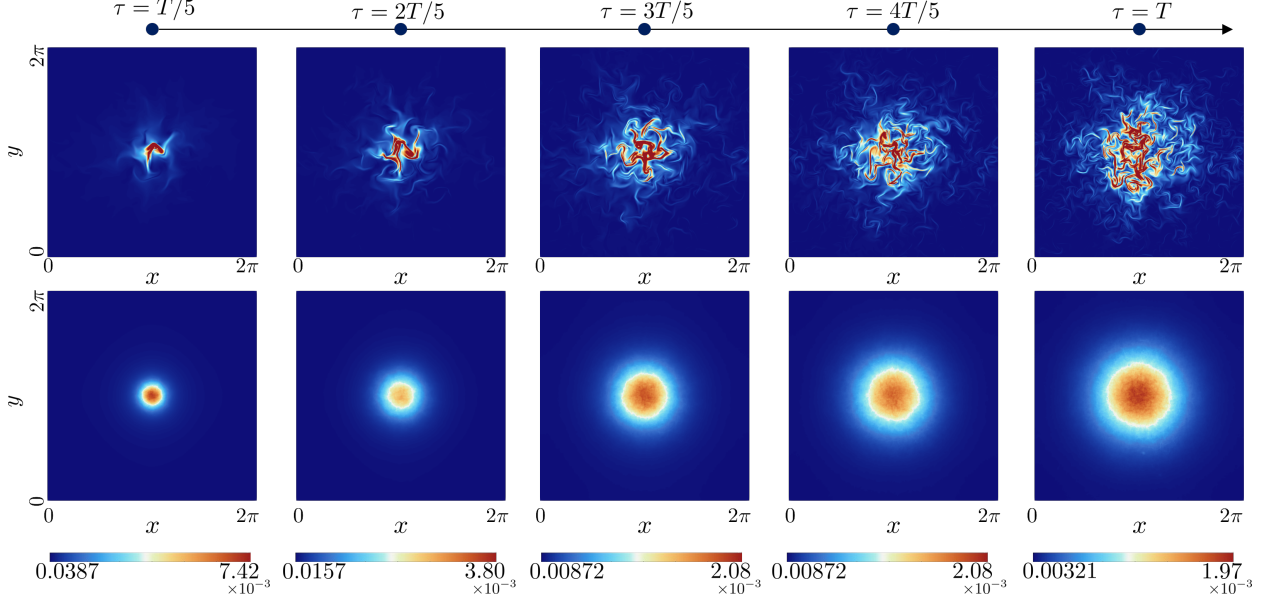


FIG. 13: Top row: Randomly selected sample from the ensemble. Bottom row: Ensemble-averaged domain of dependence for the adjoint field. Colored contours show the magnitude of the adjoint velocity vector, $|\mathbf{u}^\dagger|$.

Figure 14(a) shows the shell-averaged adjoint energy spectra, indicating that adjoint energy is broadband and evolves non-uniformly across wavenumbers during backward integration. Figure 14(b) presents the temporal evolution of the total adjoint energy, defined as the spatial L^2 norm of the adjoint velocity field. Two ensemble statistics are shown: the energy of the ensemble-mean adjoint field, obtained by first averaging $\mathbf{u}^\dagger(\mathbf{x}, \tau)$ across realizations and then computing its spatial energy, and the ensemble-averaged adjoint energy, obtained by averaging the spatial energy of each realization. The comparison highlights the contrasting behaviors of the mean component and the variance-dominated component of adjoint energy during backward integration.

Near $\tau = 0$ or $t = T$, both quantities decay exponentially in time because diffusion dominates for a broadband perturbation. After the initial transient region (for a time period around 0.3), the red solid curve shows that the averaged adjoint energy, or variance $\|\mathbf{u}^\dagger\|^2$, grows exponentially in backward time, confirming the chaotic divergence of trajectories. In contrast, the blue solid curve ($\|\overline{\mathbf{u}^\dagger}\|^2$) shows exponential decay even after the transient region. This contrast highlights the fundamental difficulty in both optimization and the estimation of ensemble-averaged sensitivity: while the mean decays exponentially, the variance grows exponentially, implying that an exponentially increasing number of samples is required to

maintain statistical convergence [19, 51], as further indicated by the signal-to-noise ratio $\|\overline{\mathbf{u}^\dagger}\|^2 / \|\mathbf{u}^\dagger\|^2$ shown in black dashed curves. Near the time $t = 0$, or $\tau = T - t = 2$, the mean adjoint fields also exhibit growth in energy. This behavior arises from the randomized initial condition used in the forward simulation, which dominates the diffusive effects and leads to amplified adjoint sensitivity at later backward times.

To illustrate the convergence of these statistics, we include lighter-colored lines in the background of panel (b), representing the statistics calculated from smaller subsets of the ensemble. As the sample size increases, these curves converge toward the solid lines. For chaotic systems, achieving full statistical convergence for the ensemble mean is difficult. For the current two-dimensional system, although our final ensemble size is limited by local computational resources, the calculated $\|\overline{\mathbf{u}^\dagger}\|^2$ and $\|\overline{\mathbf{u}^\dagger}\|^2$ clearly converge to the thick lines with 3000 samples.

To pinpoint the non-uniform evolution of the adjoint energy across wavenumber space, figure 15 displays the shell-wise evolution of the energy of the mean ($E^\dagger(k, \tau) = \|\overline{\hat{\mathbf{u}}^\dagger}(k, \tau)\|^2$) and the mean of the energy (variance $\|\overline{\hat{\mathbf{u}}^\dagger}(k, \tau)\|^2$) as a function of wavenumber. The results demonstrate an interesting scale dependence of adjoint sensitivity in backward time. For large-scale motions (low wavenumbers), the adjoint energy exhibits only weak temporal variation. At small scales (high wavenumbers), the total adjoint energy experiences rapid amplification for both the mean and the variance. This divergence indicates that adjoint sensitivities at high wavenumbers are overwhelmed by incoherent growth associated with small-scale instabilities, rendering the corresponding gradient information unstable for numerical optimization. Physically, this spectral analysis provides compelling evidence that the “reverse butterfly effect” in the adjoint equation manifests primarily at small scales. The high-wavenumber components of the standard adjoint field are essentially noise that obscures the valuable low-wavenumber gradient information. This observation provides the physical justification for the preconditioning strategy proposed in this work: by damping the high-wavenumber components in the gradient definition, we can filter out the chaotic noise while preserving the reliable large-scale sensitivity, thereby improving the convergence and accuracy of the data assimilation.

The spectral analysis presented above reveals a fundamental barrier in adjoint-based data assimilation for turbulent flows. We observe a “spectral catastrophe” where the adjoint energy cascades to small scales (high k) while the coherence of the sensitivity information

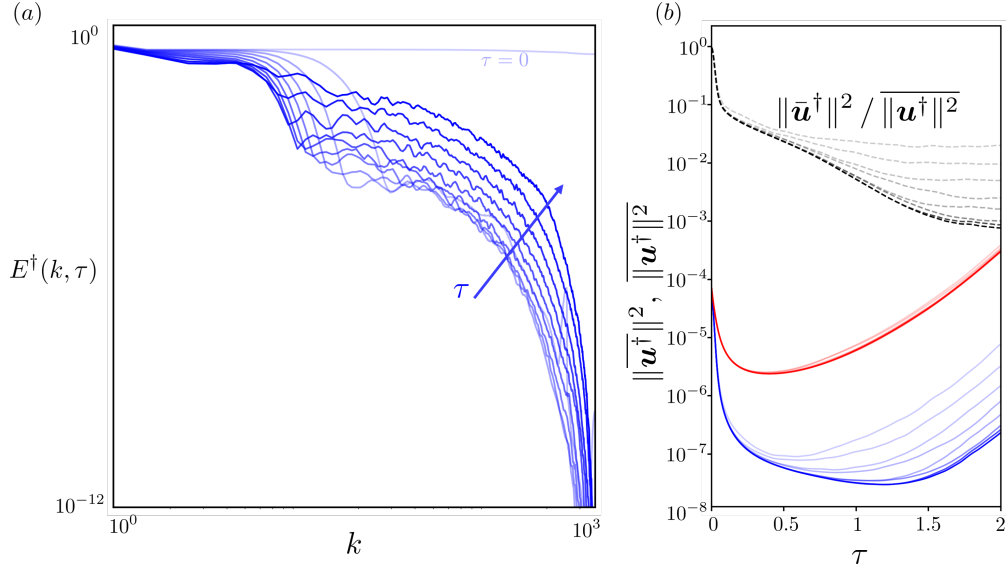


FIG. 14: (a) The energy spectra as a function of $\mathbf{k} = (k_x, k_y)$. Energy spectra from the converged ensemble adjoint approach. The curves represent the temporal evolution of the energy spectrum, with lighter shades indicating later times (t from 0.2 to 2, with a gap of 0.2). Both axes are plotted on logarithmic scales. (b) Convergence of the ensemble adjoint method. Squared norm of the ensemble-averaged adjoint fields ($\|\bar{u}^\dagger\|^2$, blue solid lines), ensemble average of the adjoint energy ($\|\bar{u}^\dagger\|^2$, red solid lines), and their ratio as a function of backward time. The convergence history uses ensemble subset sizes from 50 to 3000 samples $\{50, 100, 200, 400, 600, 1000, 2000, 3000\}$; the lighter-colored lines indicate results obtained with fewer samples, converging toward the solid lines (largest ensemble).

simultaneously vanishes. This has critical implications for the optimization problem formulated in §II. In the standard adjoint approach, which relies on the L^2 inner product, the gradient is defined based on the total adjoint energy. Consequently, the optimization direction is dominated by the high-wavenumber components-precisely those scales that represent chaotic noise rather than physical sensitivity. This explains the poor reconstruction quality and convergence issues often encountered in standard adjoint data assimilation. To address this issue, the framework provided here refines the gradient to capture the physically meaningful behavior. This requires a data-informed design of the preconditioner \mathcal{G} that properly attenuates the weighting on high-wavenumber components while retaining the large-scale components for which the gradient remains reliable. This physical insight motivates the preconditioning strategies developed in the present work and points toward further

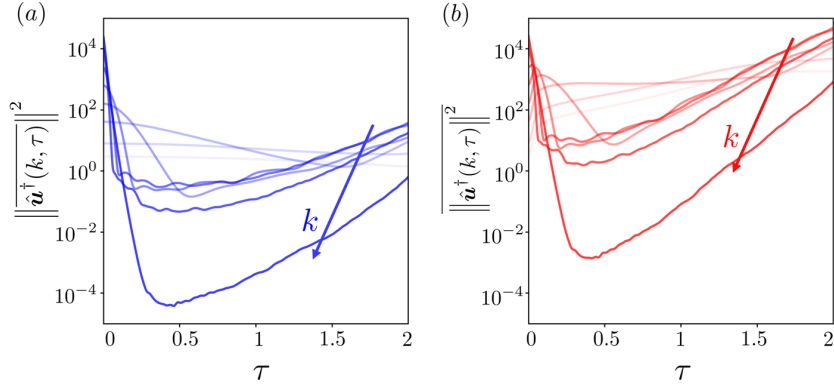


FIG. 15: Shell-wise adjoint statistics for wavenumbers $k \in \{2, 4, 8, 16, 32, 64, 128, 256\}$.

Panel (a) shows $\|\hat{\mathbf{u}}^\dagger(k, \tau)\|^2$, the energy of the ensemble-averaged adjoint in each wavenumber shell. Panel (b) shows $\|\hat{\mathbf{u}}^\dagger(k, \tau)\|^2$, the mean per-trial shell energy (3000 samples). For both panels, lighter-colored curves correspond to smaller wavenumbers k .

approaches that explicitly exploit the spectral structure of adjoint energy growth.

V. CONCLUSION

In this study, we developed a mathematical framework for preconditioned adjoint data assimilation, specifically designed to address the challenges of reconstructing chaotic turbulent flows from sparse observations. The method relies on a generalized definition of the inner product in the optimization, which introduces a spectral weighting kernel. This formulation allows for the choice of control variables in a latent space, distinct from the physical velocity space, where the simulation and optimization are more effectively performed. For the specific forms of the preconditioner being an algebraic or exponential weighting in wavenumber space, this approach can be interpreted as using the fractional derivative, or a sharpened version of the velocity as a control vector for the optimization. Employing the preconditioner implicitly introduces a precursor simulation step, similar to solving a diffusion equation within the data assimilation loop, and helps regularize the ill-posed inverse problem. Our results demonstrate that this preconditioning could significantly improve reconstruction accuracy. The exponential preconditioner, which mimics the physics of the heat equation, proved particularly effective. It acts as a robust smoother that stabilizes the optimization by suppressing high-wavenumber instabilities while retaining the fidelity

of the reconstructed flow fields. This confirms that performing the inversion in a diffusion-regularized latent space yields superior convergence and accuracy compared to standard techniques.

Finally, we clarified the source of the effect for the preconditioned adjoint by statistically examining the adjoint sensitivity. We found that, under the standard formulation, adjoint energy exhibits exponential growth, particularly at small scales due to chaotic divergence; however, this growth is largely driven by incoherent small-scale fluctuations with a negligible signal-to-noise ratio. The preconditioned approach overcomes this limitation by explicitly suppressing these unreliable high-wavenumber components. By steering the gradient descent toward coherent large-scale structures where the sensitivity remains physically meaningful, the method avoids the “spectral catastrophe” inherent to the raw adjoint and enables stable data assimilation in chaotic regimes.

Despite the improvements demonstrated here, this is a foundational work that requires further studies. First, the application to 3D turbulence remains open: while this study demonstrates the efficacy of spectral preconditioning in 2D decaying turbulence, the performance of the method in 3D flows—where the forward energy cascade and vortex stretching dominate—remains to be investigated. Second, although the exponential preconditioner proves robust, the selection of the optimal filter scale currently depends on the observation density and the Reynolds number; a self-adaptive mechanism for scale selection is a subject for future work. Third, while preconditioning effectively filters incoherent sensitivities, it does not fundamentally bypass the shadowing limits of chaotic systems over extremely long time horizons. Finally, all parameter choices in this study—including β , α , and λ —were obtained through discrete scanning rather than an analytical characterization of optimality; as a result, the reported “best” parameters reflect empirical tuning within a finite search space rather than a closed-form understanding of how preconditioning interacts with flow physics and observation structure.

Appendix A: Filtered adjoint equations

We show here that defining the adjoint with respect to the modified inner product

$$\langle \mathbf{a}, \mathbf{b} \rangle = \int_0^T \int_{\Omega} \mathbf{a}^\top \mathcal{G}^{-1} \mathbf{b} d\Omega dt$$

naturally leads to a filtered form of the adjoint equations.

Let $\tilde{\mathbf{u}}^\dagger = \mathcal{G}\mathbf{u}^\dagger$ and $\tilde{p}^\dagger = \mathcal{G}p^\dagger$ denote the filtered adjoint velocity and pressure. For any linear operator \mathcal{N} , we obtain,

$$\begin{aligned}
\langle \mathcal{N}\mathbf{u}, \tilde{\mathbf{u}}^\dagger \rangle &= \int_0^T \int_\Omega (\mathcal{N}\mathbf{u})^\top \mathcal{G}^{-1} \tilde{\mathbf{u}}^\dagger d\Omega dt \\
&= \int_0^T \int_\Omega (\mathcal{N}\mathbf{u})^\top \mathbf{u}^\dagger d\Omega dt \\
&= \int_0^T \int_\Omega \mathbf{u}^\top \mathcal{N}^\dagger \mathbf{u}^\dagger d\Omega dt \\
&= \int_0^T \int_\Omega \mathbf{u}^\top \mathcal{G}^{-1} \mathcal{G}(\mathcal{N}^\dagger \mathbf{u}^\dagger) d\Omega dt \\
&= \langle \mathbf{u}, \widetilde{\mathcal{N}^\dagger \mathbf{u}^\dagger} \rangle.
\end{aligned} \tag{A1}$$

Thus, the adjoint operator with respect to the modified inner product corresponds to the filtered version of the classical adjoint operator.

Since the filter \mathcal{G} is assumed to be symmetric and translation-equivariant in space, it commutes with spatial and temporal derivatives. Consequently, the filtered adjoint equations follow directly from the standard adjoint system.

Repeating the adjoint derivation using the modified inner product and the Lagrange multiplier $\tilde{\mathbf{u}}^\dagger$ and \tilde{p}^\dagger yields the filtered adjoint system

$$\begin{aligned}
\frac{\partial \tilde{\mathbf{u}}^\dagger}{\partial(-t)} + \widetilde{\nabla \mathbf{u} \cdot \mathbf{u}^\dagger} - \widetilde{(\mathbf{u} \cdot \nabla) \mathbf{u}^\dagger} &= \nabla \tilde{p}^\dagger + \nu \nabla^2 \tilde{\mathbf{u}}^\dagger + \mathcal{G} [\mathcal{M}^\top (\mathcal{M}(\mathbf{u}) - \mathbf{m})] - \delta(t) \lambda \nabla^2 \tilde{\mathbf{u}}_0, \\
\nabla \cdot \tilde{\mathbf{u}}^\dagger &= 0.
\end{aligned} \tag{A2}$$

These equations are precisely the filtered form of the classical adjoint system (9). The nonlinear terms appear in filtered form, e.g. $\widetilde{\nabla \mathbf{u} \cdot \mathbf{u}^\dagger}$ and $\widetilde{(\mathbf{u} \cdot \nabla) \mathbf{u}^\dagger}$, and would in general require a closure model if one were to express them solely in terms of the filtered adjoint variable $\tilde{\mathbf{u}}^\dagger$.

[1] Y. Mo and L. Magri, *Physical Review Fluids* **10**, 034901 (2025).

[2] S. Angriman, P. Cobelli, P. D. Mininni, M. Obligado, and P. Clark Di Leoni, *The European Physical Journal E* **46**, 13 (2023).

[3] X.-L. Zhang, H. Xiao, G.-W. He, and S.-Z. Wang, *Computers & Fluids* **224**, 104962 (2021).

[4] K. Duraisamy, G. Iaccarino, and H. Xiao, *Annual review of fluid mechanics* **51**, 357 (2019).

[5] T. A. Zaki, *Annual Review of Fluid Mechanics* **57**, 311 (2025).

[6] C. He, X. Zeng, P. Wang, X. Wen, and Y. Liu, *Journal of Fluid Mechanics* **978**, A14 (2024).

[7] R. Daley, *Journal of the Meteorological Society of Japan. Ser. II* **75**, 319 (1997).

[8] T. M. Hamill, *Predictability of weather and climate* **124**, 156 (2006).

[9] M. A. Ahmed and S. S. Li, *River Research and Applications* (2025).

[10] D. E. Ozan, A. Nóvoa, G. Rigas, and L. Magri, arXiv preprint arXiv:2506.01755 (2025).

[11] L. Gutierrez and Q. Wang, in *AIAA SCITECH 2026 Forum* (2026) p. 0682.

[12] K. Zhou and S. J. Grauer, arXiv preprint arXiv:2311.09076 (2023).

[13] K. Zhou and S. J. Grauer, arXiv preprint arXiv:2510.00479 (2025).

[14] F.-X. L. Dimet and O. Talagrand, *Tellus A: Dyn. Meteorol. Oceanogr.* **38**, 97 (1986).

[15] P. S. Mahar and B. Datta, *Journal of water resources planning and management* **123**, 199 (1997).

[16] P. Courtier and F. Rabier, *Atmosphere-Ocean* **35**, 303 (1997).

[17] Z. You and Q. Wang, arXiv preprint arXiv:2601.06304 (2026).

[18] Q. Wang and T. A. Zaki, *Journal of Fluid Mechanics* **1009**, A67 (2025).

[19] Q. Wang, M. Wang, and T. A. Zaki, *Journal of Fluid Mechanics* **941**, A48 (2022).

[20] S. Scott Collis, K. Ghayour, M. Heinkenschloss, M. Ulbrich, and S. Ulbrich, *International journal for numerical methods in fluids* **40**, 1401 (2002).

[21] B. Protas, T. R. Bewley, and G. Hagen, *Journal of Computational Physics* **195**, 49 (2004).

[22] A. Garai and S. M. Murman, *AIAA Journal* **59**, 2001 (2021).

[23] M. Wang, Q. Wang, and T. A. Zaki, *Journal of Computational Physics* **396**, 427 (2019).

[24] L. Gutierrez and Q. Wang, in *AIAA SCITECH 2026 Forum* (2026) p. 0510.

[25] Q. Wang, Y. Hasegawa, and T. A. Zaki, *Journal of Fluid Mechanics* **870**, 316 (2019).

[26] M. Fisher and H. Auvinen, in *Proceedings of the ECMWF Seminar Series on Data assimilation for atmosphere and ocean* (2011) pp. 6–9.

[27] Z. You, Q. Wang, and X. Zhu, in *AIAA SCITECH 2026 Forum* (2026) p. 2343.

[28] Y. Du and Q. Wang, in *AIAA SCITECH 2026 Forum* (2026) p. 1112.

[29] V. Mons, J.-C. Chassaing, and P. Sagaut, *Journal of Fluid Mechanics* **823**, 230 (2017).

[30] T. A. Zaki and M. Wang, *Phys. Rev. Fluids* **6**, 100501 (2021).

[31] N. Nikitin, *Journal of Fluid Mechanics* **849**, 942 (2018).

- [32] M. Hassanaly and V. Raman, *Physical Review Fluids* **4**, 114608 (2019).
- [33] S. Wang, Y. Teng, and P. Perdikaris, *SIAM Journal on Scientific Computing* **43**, A3055 (2021).
- [34] G. S. Alberti, E. De Vito, M. Lassas, L. Ratti, and M. Santacesaria, *Advances in Neural Information Processing Systems* **34**, 25205 (2021).
- [35] P. Korn, *Journal of Scientific Computing* **79**, 748 (2019).
- [36] M. Heinkenschloss and L. N. Vicente, *ACM Transactions on Mathematical Software (TOMS)* **25**, 157 (1999).
- [37] N. Chandramoorthy, P. Fernandez, C. Talnikar, and Q. Wang, *AIAA Journal* **57**, 4514 (2019).
- [38] V. Mons, Q. Wang, and T. A. Zaki, *Journal of Computational Physics* **398**, 108856 (2019).
- [39] A. Cleary, Q. Wang, and T. A. Zaki, [arXiv preprint \(2025\)](https://arxiv.org/abs/2512.15470), arXiv:2512.15470 [physics.flu-dyn].
- [40] Y. Wang, H. Yao, and S. Zhao, *Neurocomputing* **184**, 232 (2016).
- [41] P. Bauweraerts and J. Meyers, *Journal of Fluid Mechanics* **906**, A17 (2021).
- [42] T. Suzuki and Y. Hasegawa, *Journal of Fluid Mechanics* **830**, 760 (2017).
- [43] J. G. von Saldern, J. M. Reumschüssel, T. L. Kaiser, M. Sieber, and K. Oberleithner, *Physics of Fluids* **34** (2022).
- [44] S. Ehlers, N. Hoffmann, T. Tang, A. H. Callaghan, R. Cao, E. M. Padilla, Y. Fang, and M. Stender, *Physical Review Fluids* **10**, 094901 (2025).
- [45] Y. Hao, C. Meneveau, and T. A. Zaki, *Physical Review Fluids* **10**, 094905 (2025).
- [46] H. Moazzami, A. Jamali, N. Kevlahan, and R. A. Vargas-Hernández, [arXiv preprint arXiv:2509.22949 \(2025\)](https://arxiv.org/abs/2509.22949).
- [47] L. Huang, L. Gianinazzi, Y. Yu, P. D. Dueben, and T. Hoefler, [arXiv preprint arXiv:2401.05932 \(2024\)](https://arxiv.org/abs/2401.05932).
- [48] H. Wang, J. Han, W. Fan, W. Zhang, and H. Liu, [arXiv preprint arXiv:2505.12882 \(2025\)](https://arxiv.org/abs/2505.12882).
- [49] F. Rozet and G. Louppe, *Advances in Neural Information Processing Systems* **36**, 40521 (2023).
- [50] G. Eyink, T. Haine, and D. Lea, *Nonlinearity* **17**, 1867 (2004).
- [51] Q. Wang, *Journal of Computational Physics* **235**, 1 (2013).
- [52] J. Nocedal, *Mathematics of computation* **35**, 773 (1980).
- [53] D. C. Liu and J. Nocedal, *Mathematical programming* **45**, 503 (1989).
- [54] J. Kim and P. Moin, *Journal of computational physics* **59**, 308 (1985).
- [55] Y. Du and T. A. Zaki, *Journal of Fluid Mechanics* **1015**, A9 (2025).